CALIBRATION OF POST-LIQUEFACTION SHEAR DEFORMATION FOR A FLUVIAL DEPOSIT IN THE CHI-CHI EARTHQUAKE

P. C. Bassal[(1)], R. W. Boulanger[(2)], J. T. DeJong[(3)], and K. Ziotopoulou[(4)]

[(1)] *Graduate Student Researcher, University of California, Davis; pcbassal@ucdavis.edu*
[(2)] *Professor, University of California, Davis; rwboulanger@ucdavis.edu*
[(3)] *Professor, University of California, Davis; jdejong@ucdavis.edu*
[(4)] *Assistant Professor, University of California, Davis; kziotopoulou@ucdavis.edu*

Abstract

The performance of a two-dimensional (2D) nonlinear dynamic analysis (NDA) for a case history site of an interlayered soil deposit is evaluated under different constitutive model calibrations to understand the influence of post-liquefaction shear strain accumulation rates on the overall system response. The site is adjacent to a meandering stream channel in Wufeng, Taiwan and exhibited over two meters of liquefaction-induced ground displacements (i.e., lateral spreading) during the 1999 Chi-Chi Earthquake. In-situ data from borings and cone penetration tests (CPTs) at the site depict thinly interlayered floodplain deposits interrupted by laterally discontinuous channel fill sand deposits, typical of a fluvial point bar sequence. A majority of the floodplain deposits can be characterized as "intermediate" (e.g., low-plasticity sandy silts and clays, and silty sands) and may exhibit behavior that is transitional between sand-like and clay-like soils during cyclic loading. The subsurface is simulated using three-dimensional (3D) transition probability-based indicator geostatistics, conditioned on available data and geological inferences, for three soil categories based on state-of-practice soil behavior type index (I_C) boundary values. The 2D NDAs are performed using the PM4Sand and PM4Silt constitutive models within the FLAC finite difference program along an interpreted subsurface transect perpendicular to the stream channel. Liquefaction at this site is believed to have occurred early during seismic excitation, while a significant amount of the observed ground deformations occurred during the subsequent post-liquefaction period of ground shaking. The PM4Sand model, used for all elements representing sand-like soils, is calibrated for two significantly different post-liquefaction shear strain accumulation regimes and the system level NDA results for both calibrations are compared. The NDAs are evaluated for their ability to predict the spatial trend of ground displacements observed near the channel face. The results provide insights on the mechanistic contributions of post-liquefaction shear deformations and their ultimate influence on lateral spreading predictions for interlayered deposits.

Keywords: liquefaction; dynamic system response; constitutive modeling; interlayered deposits; lateral spreading

1. Introduction

Nonlinear dynamic analyses (NDAs) for case study sites with interlayered soil deposits have been shown to reasonably predict observed ground deformations due to earthquake-induced liquefaction (i.e. lateral spreading) and cyclic softening for reasonable parametric assumptions [e.g., 1, 2, 3]. NDAs can account for site-specific ground motions, cyclic stress-strain responses, and groundwater diffusion, all within a realistic framework that can capture a dynamic fully coupled soil-fluid response. When performed in two- or three-dimensions (2D or 3D), NDAs can incorporate details of the subsurface stratigraphy and overall site geometry to predict complex ground deformation patterns and other spatially distributed effects. As such, NDAs provide a more complete consideration of the complex system response contributing to lateral spreading than simplified empirical and semi-empirical methods [e.g., 4, 5]. However, the predictive accuracy of NDAs depends, among other factors, on their ability to realistically model the constitutive responses of the soil elements.

The selection and calibration of constitutive models for saturated sand-like soils undergoing cyclic loading should ideally capture the mechanisms of both (1) liquefaction triggering, and (2) post-liquefaction deformations. In the absence of advanced laboratory tests [e.g., cyclic direct simple shear (DSS), cyclic triaxial tests] obtained from high quality site-specific samples, constitutive models must typically be calibrated based on measurements from in-situ logging tests [e.g., cone penetration tests (CPTs) and borings]. Such in-situ tests are often the best available data for low- and moderate-risk projects, where more costly testing would not be justified [6]. Several empirical correlations with in-situ data exist for interpreting cyclic resistance to liquefaction triggering. Tasiopoulou et al. [7] recently considered a similar framework for interpreting deformations subsequent to triggering. Their study compiled the results of cyclic DSS and hollow cylinder laboratory tests on clean sands and exposed a strong trend relating post-liquefaction shear strain rate normalized by cyclic shear stress per load cycle ($\Delta\gamma_{postliq\ per\ cycle}/\tau_{cyc}$; defined as compliance rate) to the relative density (D_R). Tasiopoulou et al. demonstrated the application and utility of the proposed framework via two system-level simulations: one of a submerged tunnel surrounded by a liquefiable fill and foundation course wherein the uplift deformations are controlled by the ratcheting of the liquefiable soils, and one of a sheet pile quay wall retaining liquefiable backfill wherein the lateral deformations of the wall are controlled by the progressive accumulation of lateral strains in the backfill. While this framework shows great promise in improving model calibrations for post-liquefaction shear deformations, NDAs on a broad range of well-documented case studies are needed to understand the effects of such calibrations on predicted ground deformations. In addition, it is important to consider that there are scenarios where the system-level response is insensitive to the cyclic mobility regime, for example when the onset of liquefaction alone mobilizes a broader and distinct failure mechanism [e.g., 2] or the softening of a liquefied stratum significantly reduces dynamic stresses such that there is no significant cyclic mobility.

The overall effect of constitutive model calibrations on the system-scale response is further complicated for interlayered sites, where the sedimentary stratigraphy consists of alternating layers of different compositions (e.g., sands, silts, and clays). Such sites are affected by several limitations that may contribute to incorrect predictions of liquefaction and cyclic softening effects. These limitations are related to the site characterization tools and methods, triggering and deformation correlations, and analyzed mechanisms [8]. Any improvements in ascertaining the soil constitutive response at such sites may be overshadowed by other, more critical, limitations.

This paper considers the results of a 2D NDA study for a site adjacent to a meandering stream channel in Wufeng, Taiwan where the soil profile is interlayered and composed of floodplain deposits with "intermediate" soil beds (e.g., low-plasticity silty sands and silts) and laterally discontinuous channel sand deposits. The site performance in the 1999 Chi-Chi Earthquake, in-situ investigation data, subsurface geostatistical interpretations, and assumptions considered for a FLAC finite difference model [9] are first briefly described. An NDA study of this site was first introduced in Bassal et al. [3]; additional details regarding the site data and model building assumptions are considered in that study. Two separate calibrations of post-liquefaction shear strain accumulation rates for all sand-like soils at the site are considered for this current

study. The NDA results for both sets of calibrations provide insights on the contributions of post-liquefaction shear deformations and their ultimate influence on lateral spreading predictions for interlayered deposits.

2. Wufeng Site C

The Chi-Chi earthquake (M_W 7.6) occurred on September 21, 1999 and produced widespread permanent ground deformations throughout several inland urban centers and coastal areas due to surface faulting, landslides, and liquefaction effects [10]. Surface faulting occurred immediately to the east of the urban village of Wufeng, which experienced a peak ground acceleration of at least 0.67 g based on local seismic recording stations [11]. The urban center of Wufeng is built over an alluvial plain and is traversed by the braided Tsao-Hu River at the north, the braided Dry Creek River at the west, and several small meandering streams, including Ger-Niao-Ken Creek. A rice paddy site located at a juncture between Chung-Cheng road and the Ger-Niao-Ken Creek channel, hereafter designated as "Wufeng Site C," experienced moderate lateral spreading towards the channel. A site plan of Wufeng Site C is depicted in Fig. 1, with indicated ground crack locations and lateral spreading displacements based on field measurements and aerial photographs [12]. Along section A-A′, measured lateral displacements are directed towards the channel, commence at about 15 m from the channel edge, and range from 0.4 to 2.1 m. Based on photographs, it is assumed that the channel had side slopes of 1.8H: 1V, a base width of 6 m, and a depth of 3.2 m along Section A-A′. A minor downgrading site slope of ~0.25% to the west is assumed from available data. Also, the channel edge was lined with mortar and stones, and is assumed to cover a zone of compacted soil extending 1 to 2 m behind the channel lining.

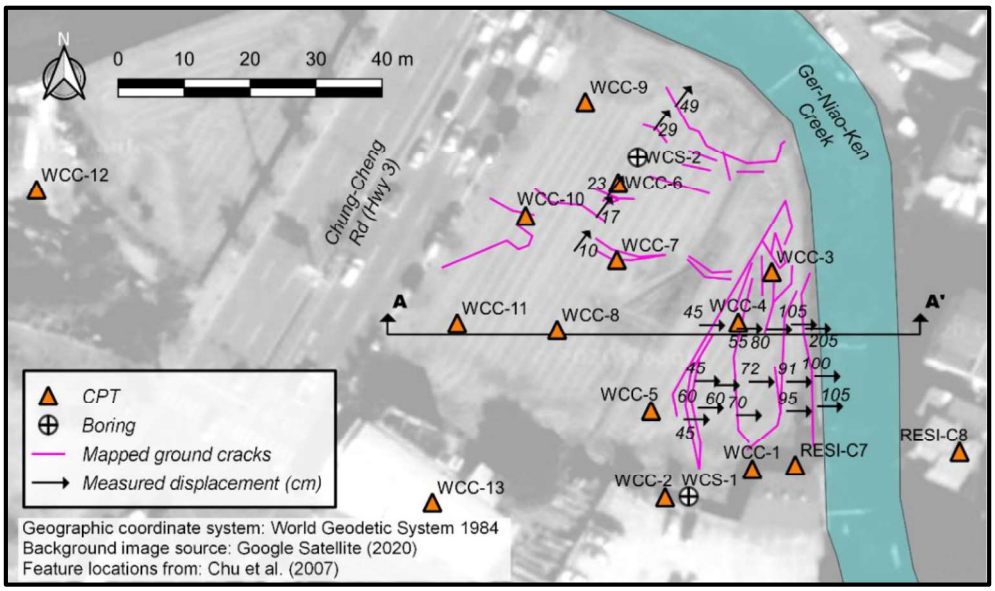

Fig. 1 – Wufeng Site C investigation plan with post-earthquake observations (adapted from Chu et al. [12] and Bassal et al. [3]). Background image from [13]. Made in QGIS.

Fifteen CPT soundings and two borings were performed at Wufeng Site C within the three years following the earthquake, as mapped in Fig. 1. Details of the site investigation are discussed in Chu et al. [14] and all data was obtained from PEER [15]. The subsurface profile in Fig. 2 shows the measured data from CPTs near section A-A′. The cone tip resistance normalized by atmospheric pressure (q_{tN}) is plotted with depth for each CPT. The CPTs readings are color-coded based on the soil behavior type index (I_C) to approximately identify layers of silt mixtures and clays ($I_C > 2.6$; blue), sand mixtures ($2.05 \leq I_C \leq 2.6$; green), and sands ($I_C < 2.05$; beige); these groupings respectively map to soil behavior types (SBTs) 3/4, 5, and 6 [16].

The subsurface layering and features of Fig. 2 were interpreted from the site data, based on a general understanding of geologic features commonly present in fluvial settings. Details regarding the stratum delineations are provided in Bassal et al. [3], with only the most pertinent details described herein. The top 1

m of the profile (stratum A) consists of surficial reworked miscellaneous sands, silts, and clays. Floodplain deposits (stratum B) exist between depths of 1 to ~15.5 m, primarily composed of silty sands interlayered with low plasticity and overconsolidated silts and clays (layers are interpreted as 10 to 50 cm thick). The floodplain deposits are often interrupted by lenses of channel-deposited sands with 0 to 20% fines. The portion of floodplain soils above the 5 m depth are observed to have lower q_{tN} values than deeper material. A soft and lightly overconsolidated clay lens is encountered in WCC-3 at a depth of 4 m, and may indicate a base for recent lateral accretion deposition from the existing channel. An overconsolidated stiff clay unit with occasional silty sand seams (stratum C) underlies stratum B to the maximum depth explored of 30 m. The groundwater level during drilling was estimated as 1 to 1.5 m below the ground surface away from the channel.

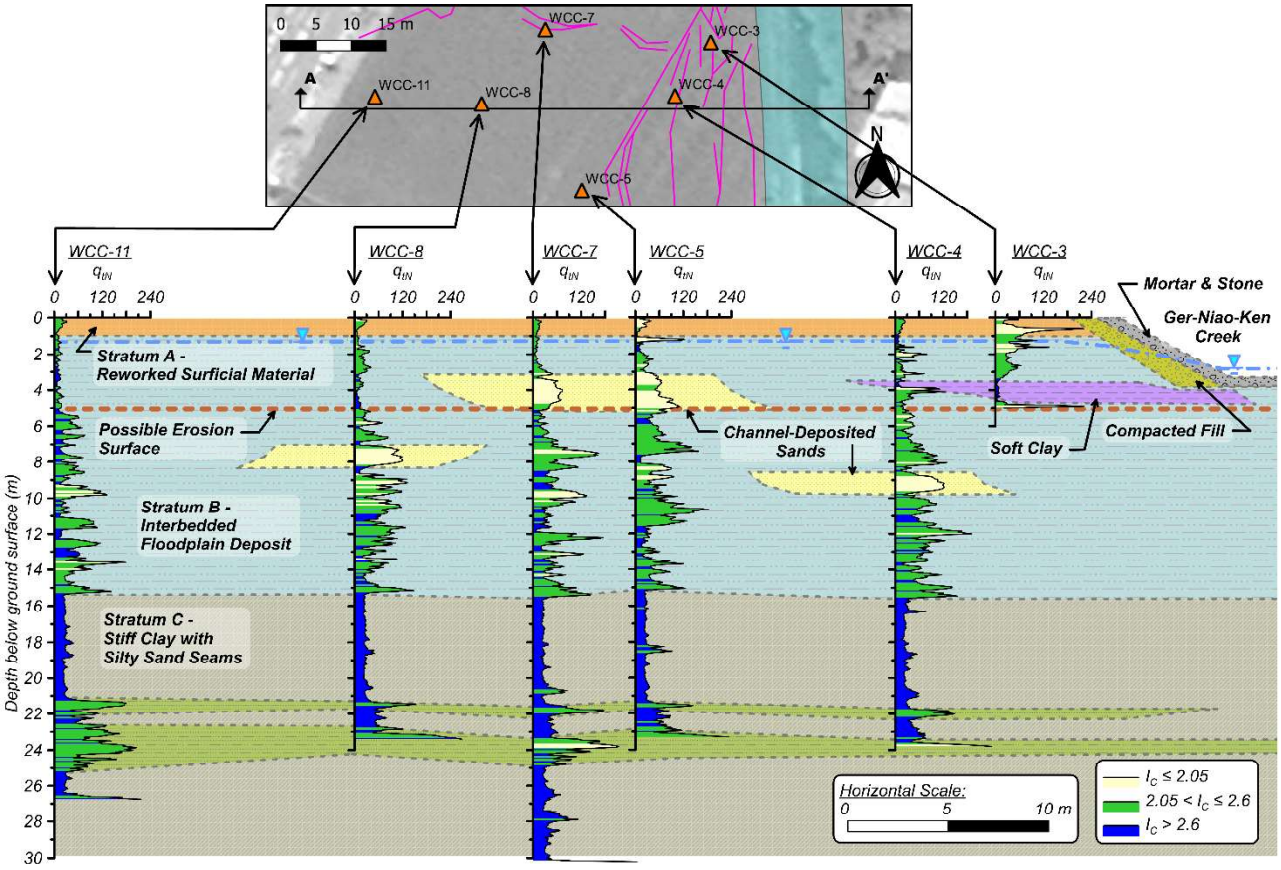

Fig. 2 – Section A-A′ CPT fence diagram with a geologically interpreted stratigraphy (adapted from [3]).

3. Nonlinear Dynamic Analyses

3.1 Geostatistical Subsurface Model

Conditional 3D simulations of stratum B were developed using the category-based transition probability software package TPROGS [17]. This geostatistical approach is advantageous for geotechnical subsurface simulations of interlayered deposits since it can be conditioned on available site investigation data and it accounts for geologically-derived attributes of distinct soil categories, including their (1) proportions, (2) mean thicknesses and lengths, and (3) relative ordering. Three categories were defined by the I_C ranges used in Fig. 2, and are labeled as B3, B5, and B6; the number indicates the most pertinent SBT [16]. In addition to being conditioned on the CPT measurements, the full stratum B thickness at the western end of the site was further conditioned as uniform B6 material, to approximate the expected behavior beyond the model extents and prevent unrealistic boundary strains during the dynamic analyses. A 2D slice along section A-A′ for one simulation of stratum B is considered for the current analysis as shown in Fig. 3.

Representative properties were determined individually for all distinct materials encountered including stratum A, stratum B (i.e., B3, B5, and B6), stratum C, the compacted zone, and the mortar and stone lining. Properties for the soil strata were derived from the CPT data after inverse filtering using the procedure of Boulanger and DeJong [18] with baseline filter parameters. Inverse filtering is expected to approximately remove thin-layer and transition zone effects, and provide more accurate parameter estimates based on q_{tN}. The normalized clean sand corrected tip resistance (q_{c1Ncs}) for the sand-like soils was calculated per Boulanger and Idriss [19] using a site-specific fines content correction conditioned on measurements from boring samples. Median (50th percentile) estimates of q_{c1Ncs} were considered from all CPTs at the site for the applicable I_C range. The stratum A surficial reworked material is assumed to have a q_{c1Ncs} of 76. The q_{c1Ncs} is estimated as 76 and 89 above a 5 m depth, and 116 and 137 below a 5 m depth, for B5 and B6, respectively. The compacted zone beside the channel is assumed to have a q_{c1Ncs} of 126; consistent with a relative density (D_R) of 65%. Two distinct peak undrained shear strength ratios (s_u/σ'_{vc}) are assumed for the B3 interlayers in the near-channel region (i.e., depths above 5 m and laterally within 10 m from the channel base) and the remainder of the profile as 0.38 and 0.76, respectively. Stratum C is assumed to extend to a depth of 30 m and have a constant undrained shear strength (s_u) of 150 kPa. The mortar and stone lining was modeled with Mohr-Coulomb properties and is assumed to have a cohesion of 20 kPa and friction angle of 10 degrees. An elastic halfspace was also assigned to the model base with a shear modulus of 304 MPa and a Poisson ratio of 0.33.

Other soil parameters were estimated based on correlations with CPT data. The saturated unit weight (UW_{sat}) is assumed as 20 kN/m^3 for stratum A and 21 kN/m^3 for all other strata, with a 15% reduction above the phreatic surface. Vertical and horizontal hydraulic conductivities were estimated per Robertson [20]. The normalized shear wave velocity (V_{s1}) was estimated for sand-like soils per Andrus et al. [21] as 165 and 177 m/s for B5 and B6 in the upper 5m, and 180 and 195 m/s for B5 and B6 below 5 m, respectively. The V_{s1} for all B3 soils was estimated as 193 m/s per Carlton and Pestana [22]. The V_{s1} in stratum C was estimated based on data at a neighboring site as 236 m/s. The V_{s1} in the elastic halfspace is 325 m/s.

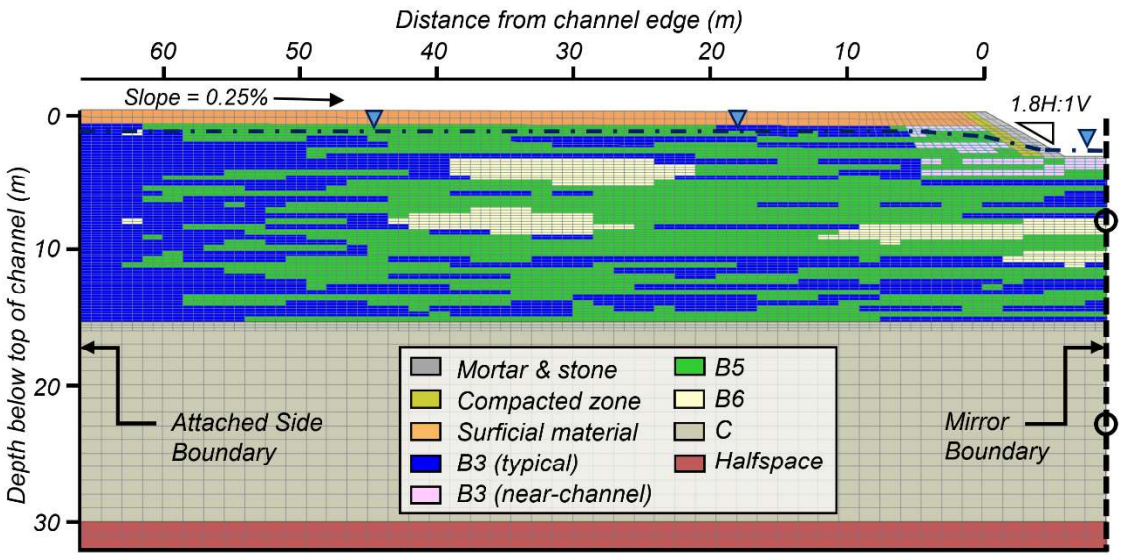

Fig. 3 – NDA "left-side" mesh as used in FLAC with simulated layering for stratum B (adapted from [3]).

The section A-A′ profile (Fig. 2) was modeled as a 2D NDA using the finite difference program FLAC 8.1 [9] and the user-defined constitutive models PM4Sand (Version 3.1; [23]) and PM4Silt (Version 1; [24]). Fig. 3 depicts the left-half of the full plane-strain mesh; the right-half of the mesh is an exact mirror image. The full model mesh is 150 m long by ~32 m tall, and is comprised of 16,896 elements. Elements are typically 0.75 m long by 0.2 m tall above a 16 m depth (except they are 0.5 m tall in Stratum A and skewed near the channel), and are 1.5 m long by 1 m tall below this depth. Stress conditions were initialized prior to dynamic loading by choosing elastic moduli that would produce a coefficient of earth pressure at rest (K_o) of 0.5 for all soil strata. The water table was initialized by setting a static phreatic surface at 1.25 m below the ground surface

outside the channel and at 0.6 m above the channel base, and allowing flow to equilibrate between these areas. The moist total density above the phreatic surface was set as 85% of the saturated total density. The water tensile strength limit was initialized at 5 kPa to allow for saturation (capillary rise) up to about 0.5 m above the phreatic surface. This limit was increased to 100 kPa during shaking to allow for transient negative pore pressure development. The boundary conditions for the dynamic analyses include a compliant (quiet) base, where the outcrop input motion is applied as a horizontal stress time history. The left and right boundaries of the full mesh (right side is not shown in Fig. 3) are attached together. Although actual soil conditions across the channel may differ, the symmetric model minimizes incongruences in soil behavior between the attached side boundaries. The mirrored right half of the model is expected to behave identically to the left half, but with a reversed ground motion polarity. Additional details regarding the geostatistical subsurface simulations, selection of representative properties, and numerical model assumptions are discussed in Bassal et al. [3].

3.2 Calibration of Constitutive Models

The PM4Sand parameters are presented in Table 1 for all sand-like soils. The shear modulus coefficient (G_o) was determined from V_{s1} and UW_{sat} at the middle of each layer. The apparent D_R was derived from the representative q_{c1Ncs} using Boulanger and Idriss [19]. The contraction rate parameter (h_{po}) was determined from single-element calibrations targeting a single-amplitude shear strain (γ) of 3% at 15 uniform stress cycles (N) of simulated undrained DSS loading, under the initial vertical effective stress (σ'_{vc}) near the center of the layer. Stress cycles equivalent to the cyclic resistance ratio ($CRR_{M7.5}$) were used for calibrating h_{po}; $CRR_{M7.5}$ was obtained based on the q_{c1Ncs} relationship by Boulanger and Idriss [19] for a 50% probability of liquefaction after overburden corrections at σ'_{vc}. To account for the post-liquefaction shear strain accumulation rate, two separate calibrations were considered for all PM4Sand materials and are herein referred to as (1) default and (2) median. The default calibration included no additional adjustment for post-liquefaction deformations beyond the PM4Sand primary input parameters (i.e., default values were used for secondary parameters). The median calibration involved adjusting the secondary parameter C_ε, until undrained DSS simulations with uniform stress cycles of $CRR_{M7.5}$ matched the empirical median post-liquefaction compliance rate ($\Delta\gamma_{post\text{-}liq\ per\ cycle}/\tau_{cyc}$) proposed by Tasiopoulou et al. [7]. While calibrating C_ε, it was also necessary to recalibrate h_{po} to maintain γ = 3% at N = 15 cycles. The compliance rates for the default and median calibrations were both evaluated at applied cyclic stress ratios (CSRs; or τ_{cyc}/σ'_{vc}) equivalent to $CRR_{M7.5}$ of 0.1 and 0.4 with the resulting ranges in Table 1. Default values were used for all other secondary parameters.

Table 1 – PM4Sand constitutive model inputs

Material	*Center* σ'_{vc} *(kPa)*	D_R	G_o	$CRR_{M7.5}$	*Default Calibration*		*Median Calibration*		
					h_{po}	$\Delta\gamma_{postliq\ per\ cycle}/\tau_{cyc}$	h_{po}	C_ε	$\Delta\gamma_{postliq\ per\ cycle}/\tau_{cyc}$
Compacted Zone	35	0.65	907	0.249	0.15	0.009 - 0.034	0.35	0.64	0.008 - 0.047
A & B5 (above 5m)	42	0.44	700	0.148	0.90	0.070 - 0.086	1.22	33.0	0.170 - 0.430
B6 (above 5m)	42	0.50	805	0.166	0.55	0.038 - 0.060	0.85	5.7	0.110 - 0.200
B5 (below 5m)	123	0.62	837	0.195	0.67	0.026 - 0.038	0.71	1.5	0.037 - 0.077
B6 (below 5m)	123	0.69	982	0.265	0.88	0.013 - 0.022	0.92	0.5	0.024 - 0.028

A comparison of the cyclic DSS behavior for the single-element default and median calibrations of the B5 soils (above 5 m) is provided in Fig. 4. Both calibrations reach single-amplitude γ = 3% at N = 15 cycles of $CRR_{M7.5}$ = 0.148. However, the rate of shear strain accumulation beyond N = 15 cycles is much larger for the median calibration, which reaches γ = 3% at N = 17 cycles as opposed to N = 26 cycles. As seen in Table 1, the compliance rate ranges for the median calibration are larger than for the default calibrations.

PM4Silt parameters used in the NDA analyses are listed in Table 2 for all clay-like soils. As for PM4Sand materials, G_o was determined from V_{s1} and UW_{sat}. The representative s_u/σ'_{vc} was increased by a 25% strain rate adjustment to obtain the undrained shear strength ratio at critical state under earthquake loading

($s_{u,cs,eq}/\sigma'_{vc}$). The shear modulus parameter (h_o) was adjusted until the simulated DSS response approximated the shear modulus reduction and equivalent damping behavior of the empirical relationship by Darendeli [25]. The h_{po} parameter was calibrated to produce a reasonable slope of CSR against N to γ = 3%. The void ratio (e_o) of the B3 and C soils was estimated from index tests. The near-channel B3 soft clays were assigned a bounding surface parameter ($n^{b,wet}$) of 0.01 and a critical state friction angle (ϕ'_{cv}) of 45 degrees to simulate a modest clay sensitivity of 1.5. Default values were used for all other secondary PM4Silt parameters.

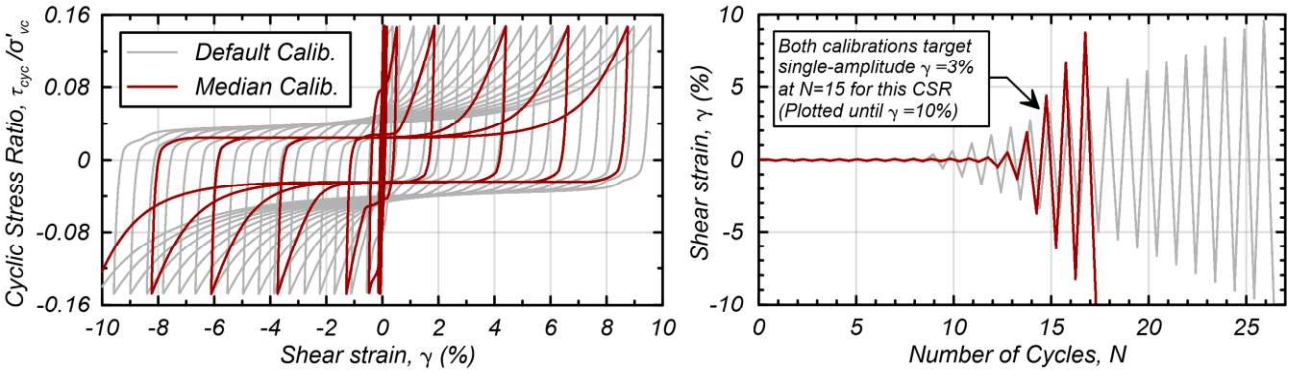

Fig. 4 – Calibration of B5 (above 5m) for default and median post-liquefaction shear strain accumulations.

Table 2 – PM4Silt constitutive model inputs

Material	$s_{u,eq,cs}/\sigma'_{vc}$	$s_{u,eq,cs}$ *(kPa)*	G_o	h_{po}	h_o	e_o	$n^{b,wet}$	ϕ'_{cv}
B3 (near-channel)	0.32	-	1030	8	0.9	0.55	0.01	45
B3 (typical)	0.95	-	1030	30	0.9	0.55	-	-
C	-	188	1250	10	1.5	0.51	-	-

3.3 Ground Motion

This study considers a single east-west trending ground motion recording of the Chi-Chi earthquake from TSMIP (Taiwan Strong Motion Instrumentation Program) strong motion station TCU067 [11], for direct input at the NDA model base. This motion reached a peak ground acceleration (PGA) of 0.50 g during the event. TCU067 is located 5 km northeast of Wufeng Site C and 350 m from the fault rupture. It is situated over stiff material with a shear wave velocity in the upper 30 m (V_{s30}) of 440 m/s [26].

4. Results

The dynamic response obtained with the default calibration for post-liquefaction shear deformations is presented in Fig. 5, which shows contours of the maximum (i.e., during shaking) excess pore pressure ratio (r_u; defined as one minus the ratio of the current to initial vertical effective stress) and shear strain (γ; defined as the engineering strain for the principal stress orientation) across the "left-side" NDA model to a depth of 16 m. By comparing the r_u contours with the soil groups (Fig. 3), a majority of the B5 silty sand liquefies (i.e., r_u near 100%), except within ~5 m to the side of and below the channel geometry. The soil beneath the channel heaves during ground shaking, with the associated shear stresses limiting the maximum attainable r_u values in this region. Of the four B6 sand lenses in this realization, only the shallowest liquefies, likely due to its calibration to a lower cyclic resistance than the deeper layers. The maximum γ contour plot (Fig. 5) shows that the largest shear strains (>300%) coincide with the B3 soft clay below the channel. The path of a rotational slump feature extends from the basal soft clay to the surface at 9 m from the channel. Strains of up to ~30% occur within several laterally continuous B5 and B6 lenses away from the channel, for depths of 1 to 15.5 m.

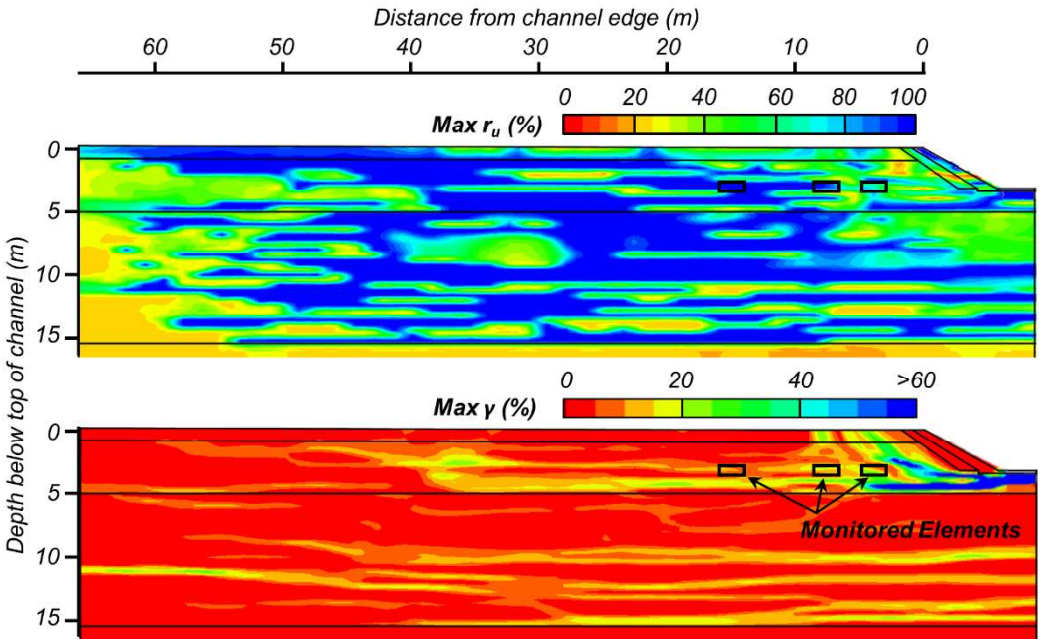

Fig. 5 – Contours of maximum r_u and γ after shaking for NDA with default shear deformation calibration.

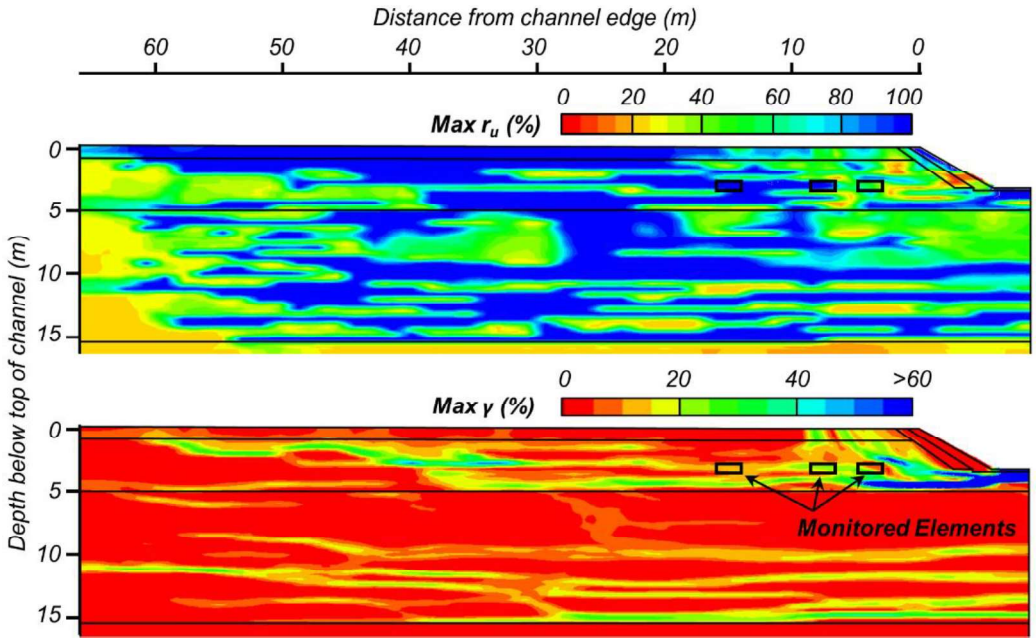

Fig. 6 – Contours of maximum r_u and γ after shaking for NDA with median shear deformation calibration.

Contours of maximum r_u and γ obtained with the median calibration for post-liquefaction shear deformations are presented in Fig. 6. The r_u contours show slightly fewer zones of liquefaction than the default calibration; particularly at depths of 5 to 7 m in the areas between 8 to 20 m and 28 to 35 m from the channel edge. The maximum γ contours depict a similar rotational slump near the channel as with the default calibration, but typically show much higher maximum strains of up to ~50% along the B5 and B6 lenses away from the channel.

Time histories of three elements, in Fig. 7, help explain some similarities and differences between results for the two shear deformation calibrations. The elements are located along a single B5 lens aligned with the channel depth (3.2 m), and positioned at 4 m (within the slump feature), 8 m (at the outer extent of the slump feature), and 15 m (away from the slump feature) from the channel edge. Time histories are shown for the total

shear stress ratio (τ_{hv}/σ'_{vc}), engineering shear strain (γ_{hv}; along a horizontal plane), and r_u during the 40 s ground motion. The τ_{hv}/σ'_{vc} applied at the base of the model is also shown. All three elements begin the motion with similar responses until a peak stress cycle at 8.8 s causes excessive dilation along the entire lens, as evidenced by negative r_u spikes. The element at 15 m cycles back into a contractive state and triggers liquefaction upon completing the stress cycle. However, the r_u for the elements at 4 and 8 m remains low after 8.8 s, likely due to the introduction of a "static" shear bias as evidenced by a baseline shift in τ_{hv}/σ'_{vc}. This shear bias is caused by stress redistribution near the zones sheared by the rotational slump. Soon after liquefaction initiates, the element at 15 m with the median calibration exhibits a more magnified cycling of γ_{hv} than the default calibration, as expected. The γ_{hv} cycling of the elements at 4 and 8 m is less pronounced, due to a rotation of the principal stresses (i.e., maximum shear is instead along an inclined plane). From ~11 s to the end of shaking, the τ_{hv}/σ'_{vc} peaks are typically lower for the median calibration in all three elements. Greater strains in shallower or deeper lenses for the median calibration (Fig. 6) are believed to have limited the available τ_{hv}/σ'_{vc} that could be transmitted to this lens, as observed in past studies of system response for layered soils [27, 28]. The final 24 seconds of milder shaking have little effect near the channel, but a large effect on the element at 15 m, as both models strain in opposing directions towards a similar final γ_{hv} of ~10%.

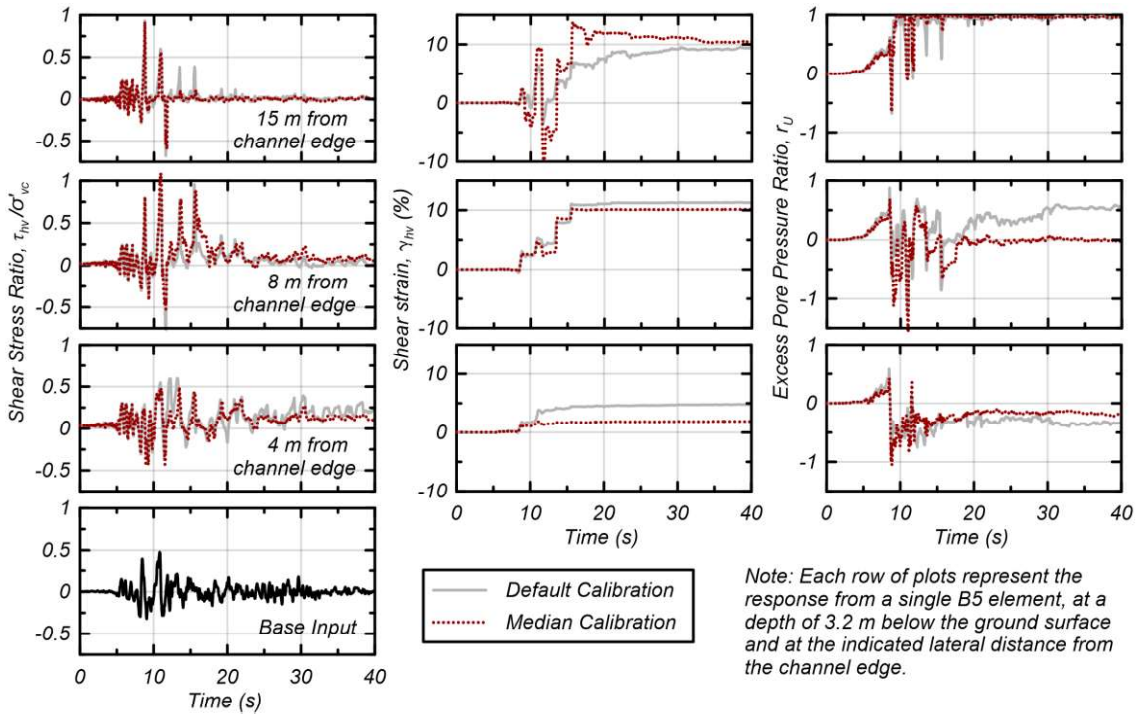

Fig. 7 – Time histories for three B5 elements from two NDAs with different shear deformation calibrations.

The stress-strain and stress path response during shaking of the element at 15 m is depicted in Fig. 8 for both calibrations. The labeled times indicate four peaks in τ_{hv}/σ'_{vc} that dominate the response. The post-liquefaction stress-strain response depicts much larger strains with the median rather than default values, for a similar τ_{hv}/σ'_{vc} at 8.8, 10.9, and 11.7 s, in agreement with the single-element calibration (Fig. 4). These peaks simultaneously produce a high amount of dilation in the element, with the normalized vertical effective stress (σ'_v/σ'_{vc}) close to or greater than one. However, as previously described, the τ_{hv}/σ'_{vc} peak values are severely reduced for the median calibration after this time. At 13.5 s, the default calibration approaches a peak τ_{hv}/σ'_{vc} of 0.38, which is much higher than the synchronous peak of 0.05 with the median calibration. This and subsequent large dilation cycles result in the default calibration gradually accumulating deformations to a magnitude similar to that exhibited by the median calibration.

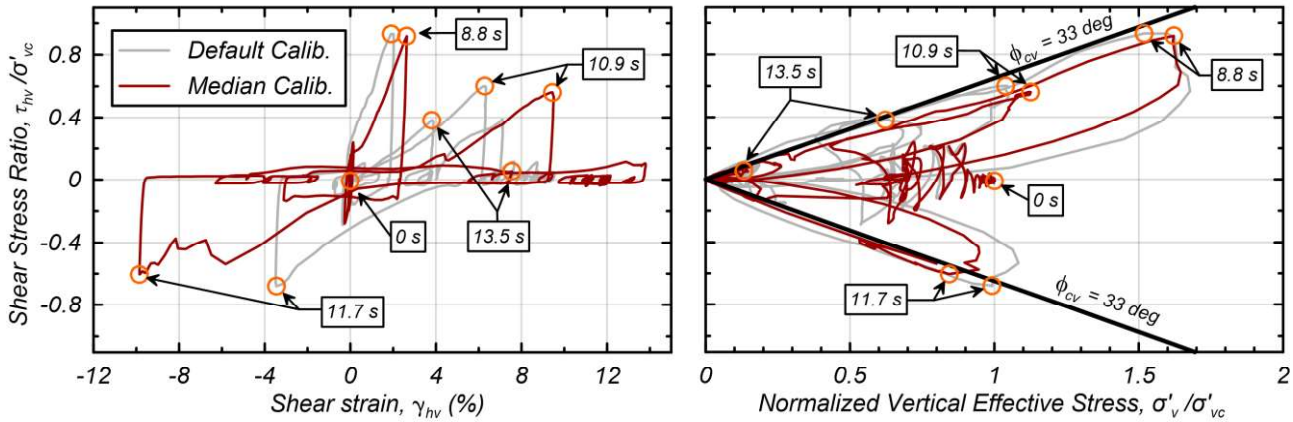

Fig. 8 – Dynamic response for one B5 element (3.2 m below top of channel; 15 m from channel edge) from two NDAs with different shear deformation calibrations.

The resulting lateral spreading towards the channel is compared against the field measurements for both calibrations at positive and negative ground motion polarities in Fig. 9. Within 20 m of the channel, computed ground deformations are consistent with the field observations. The total range of measured deformations of 45-205 cm is captured with the positive motion (70-140 cm), but slightly underestimated with the negative motion (0-80 cm) for both calibrations. All models also show a gradual reduction of deformations beyond 20 m, which was not recorded and may not have been visible in the field. Overall ground lurching of 30-40 cm extended to the model boundaries 66 m from the channel, and was oriented towards the channel for the positive motion and away from the channel for the negative motion. For each ground motion, the default and median calibrations tend to exhibit practically identical deformations within 40 m of the channel, with some slight differences of up to 20 cm further in the free field. The near-channel response is primarily dominated by the rotational slump that slips along the B3 soft clay, whereas the further regions were more affected by straining in the B5 silty sands. From these observations, it is apparent that the ground motion polarity was able to influence the resulting deformations much more significantly than the shear strain accumulation rate.

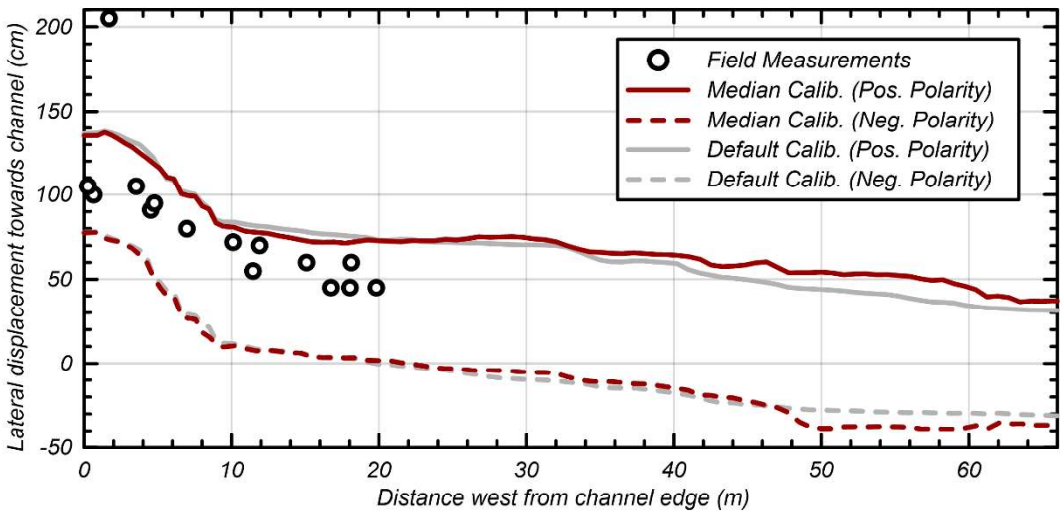

Fig. 9 – Ground deformations from field measurements and NDAs with different calibrations and polarities.

6. Conclusions

The seismic performance of the interlayered Wufeng Site C during the 1999 Chi-Chi earthquake was evaluated using 2D NDAs with FLAC [9] and the user-defined constitutive models PM4Sand and PM4Silt [23, 24], for a realization developed from a 3D transition probability geostatistical model. The PM4Sand model for all sand-

like soils was calibrated for two different post-liquefaction shear strain accumulation rate assumptions based on: (1) default parameters, and (2) median shear strain accumulation rates proposed by Tasiopoulou et al. [7] for clean sands without static stress bias. The site experienced up to 2.1 m of lateral spreading displacements adjacent to the meandering stream channel, or about 0.8 m on average within 20 m of the channel.

The geostatistical model allowed for insights on the contributions of interlayering for the shear deformations in the sand-like soils. Comparing the dynamic responses of individual elements within a critical silty sand lens of the NDAs suggested that while greater shear strain accumulation rates caused greater strains soon after liquefaction was triggered, the stresses imposed on this lens were subsequently reduced due to overall greater yielding in other layers. Both models calibrated to different shear deformation rates ultimately resulted in similar post-earthquake strains throughout the profile and lateral spreading patterns at the surface. In contrast, details of the ground motion related to the polarity and distribution of cycles largely affected the magnitude of ground deformations, particularly in the free-field away from the channel. Large deformations within 10 m of the channel were largely independent of the shear deformation calibration and were instead controlled by a rotational shearing surface exacerbated by yielding along a locally weaker clay lens.

These NDA results suggest that in the absence of advanced site-specific laboratory testing, it is meaningful to undertake a sensitivity study to determine how post-liquefaction cyclic mobility affects the computed deformations. For this site, other factors had a stronger effect on the computed deformations. Concurrent studies are evaluating the influence of the subsurface stratigraphy, material properties, input ground motions, and numerical procedures on the deformation patterns for this case history.

7. Acknowledgements

The authors appreciate the financial support of the National Science Foundation (award CMMI-1635398) and California Department of Water Resources (contract 4600009751) for different aspects of the work presented herein. Any opinions, findings, conclusions, or recommendations expressed herein are those of the authors and do not necessarily represent the views of these organizations. The authors benefited from discussions with Graham Fogg regarding transition probability geostatistics, as well as the archived data and past studies of this site by Daniel Chu, Jonathan Stewart, Leslie Youd, Bin-Lin Chu, Shannon Lee, Sung-Chi Hsu, and others.

8. References

[1] Boulanger, R. W., Munter, S. K., Krage, C. P., & DeJong, J. T. (2019). "Liquefaction evaluation of interbedded soil deposit: Çark Canal in 1999 M7.5 Kocaeli Earthquake." J. Geotech. Geoenviron. Eng., ASCE, 145(9): 05019007, /10.1061/(ASCE)GT.1943-5606.0002089.

[2] Pretell, R. A., Ziotopoulou, K., & Davis, C. (2020). Numerical modeling of ground deformations at Balboa Blvd. in the Northridge 1994 Earthquake. J. Geotech. Geoenviron. Eng., ASCE, 10.1061/(ASCE)GT.1943-5606.0002417.

[3] Bassal, P. C., Boulanger, R. W., & DeJong, J. T. (2021). "Dynamic analyses of liquefaction and lateral spreading for an interlayered deposit in the Chi-Chi earthquake." Submitted 2/19/21 for ASCE Geo-Extreme 2021, Savannah, GA.

[4] Youd, T. L., Hansen, C. M., & Bartlett, S. F. (2002). "Revised multilinear regression equations for prediction of lateral spread displacement." J. Geotech. Geoenviron. Eng., 128(12), 1007–1017.

[5] Zhang, G., Robertson, P. K., & Brachman, R. W. (2004). "Estimating liquefaction induced lateral displacements using the standard penetration test or cone penetration test." J. Geotech. Geoenviron. Eng., 130(8), 861–871.

[6] Robertson, P. K. (2009). "Interpretation of cone penetration tests - a unified approach." Can. Geotech. J. 46: 1337-1355. doi: 10.1 l39/T09-065.

[7] Tasiopoulou, P., Ziotopoulou, K., Humire, F., Giannakou, A., Chacko, J., & Travasarou, T. (2019). "Development and implementation of semiempirical framework for modeling postliquefaction deformation accumulation in sands." J. Geotech. Geoenviron. Eng. doi.org/10.1061/(ASCE)GT.1943-5606.0002179.

[8] Boulanger, R.W., Moug, D.M., Munter, S.K., Price, A.B. & DeJong, J.T. (2016). "Evaluating liquefaction in interbedded sand, silt, and clay deposits using the cone penetrometer." Proc., 5th Int. Conf. on Geotech. & Geophys. Site Char.: Queensland, Australia.

[9] Itasca (2019). "FLAC, Fast Lagrangian Analysis of Continua, User's Guide, Version 8.1." Itasca Consulting Group, Inc., Minneapolis, MN.

[10] Multidisciplinary Center for Earthquake Engineering Research (MCEER) 2000. "The Chi-Chi, Taiwan Earthquake of September 21, 1999: Reconnaissance Report." Technical Report MCEER-00-0003. University at Buffalo, State University of New York.

[11] Pacific Earthquake Engineering Research Center (PEER) (2013). "PEER Ground Motion Database: NGA-West2." retrieved 06/01/2020 from https://ngawest2.berkeley.edu/.

[12] Chu, D. B., Stewart, J. P., Youd, T. L. & Chu, B. L. (2007). "Liquefaction-induced lateral spreading in near-fault regions during the 1999 Chi-Chi, Taiwan Earthquake." J. Geotech. & Geoenv. Eng., ASCE, 132(12), 1549-1565.

[13] Google (2020). "Satellite" [basemap]. "Satellite Imagery." July 02, 2020. https:// mt1.google.com/vt/.

[14] Chu, D. B., et al. (2004). "Documentation of soil conditions at liquefaction and non-liquefaction sites from 1999 Chi-Chi (Taiwan) earthquake." Soil Dyn. Earthquake Eng., 24(9-10), 647–657.

[15] Pacific Earthquake Engineering Research Center (PEER) (2002). "Taiwan Ground Failure Database," retrieved 05/01/2020 from https://apps.peer.berkeley.edu/.

[16] Robertson, P. K., and Wride, C. E. (1998). "Evaluating cyclic liquefaction potential using the cone penetration test." Can. Geotech. J., 35(3), 442–459.

[17] Carle, S.F. (1999). "TPROGS: Transition Probability Geostatistical Software: Users Guide." Univ. of CA, Davis.

[18] Boulanger, R. W., & DeJong, J. T. (2018). "Inverse filtering procedure to correct cone penetration data for thin-layer and transition effects." Proc., Cone Penetration Testing 2018, Hicks, Pisano, & Peuchen, eds., Delft Univ. of Tech., The Netherlands, 25-44.

[19] Boulanger, R. W., & Idriss, I. M. (2014). CPT and SPT based liquefaction triggering procedures. Report No. UCD/CGM.-14/01.

[20] Robertson, P. K. (2010). "Estimating in-situ soil permeability from CPT & CPTu." Proc., 2nd Int. Symp. on Cone Penetration Testing, Huntington Beach, CA.

[21] Andrus R. D., Piratheepan, P., Ellis, B. S., Zhang, J., & Juang, C. H. (2004). "Comparing liquefaction evaluation methods using penetration-VS relationships." Soil Dynamics & Earthquake Engineering, 24, 713-721.

[22] Carlton, B. D., and Pestana, J. M. (2012). "Small strain shear modulus of high and low plasticity clays and silts." 15th World conference on earthquake engineering, Lisbon, Portugal.

[23] Boulanger, R. W., & Ziotopoulou, K. (2017). "PM4Sand (Version 3.1): A sand plasticity model for earthquake engineering applications." Report No. UCD/CGM-17/01, Center for Geotech. Modeling, Dept. of Civil and Environ. Eng., Univ. of Cal., Davis, CA, 113 pp.

[24] Boulanger, R. W., & Ziotopoulou, K. (2018). "PM4Silt (Version 1): A silt plasticity model for earthquake engineering applications." Report No. UCD/CGM-18/01, Center for Geotech. Modeling, Dept. of Civil and Environ. Eng., Univ. of Cal., Davis, CA, 108 pp.

[25] Darendeli, M. B. (2001). Development of a new family of normalized modulus reduction and material damping curves [Ph. D. dissertation]. University of Texas at Austin.

[26] Kuo, C. H., Wen, K. L., Hsieh, H. H., Lin, C. M., Chang, T. M., & Kuo, K. W. (2012). "Site Classification and Vs30 estimation of free-field TSMIP stations using the logging data of EGDT." Engineering Geology, 129-130, 68-75.

[27] Cubrinovski, M., Rhodes, A., Ntritsos, N., & van Ballegooy, S. (2018). "System response of liquefiable deposits." Soil Dynamics & Earthquake Engineering, 124, 212-229.

[28] Bassal, P. C., and Boulanger, R. W. (2021). "System Response of an Interlayered Deposit with Spatially Preferential Liquefaction Manifestations." Draft submitted January 31, 2021 to J. Geotech. Geoenviron. Eng., ASCE.

